Research Article

Yin Luo, Jianmin Wu*, Zhong Qin, and Hengcong Zhang

# $Fe^{3+}$ and $Ce^{3+}$ modified nano-$TiO_2$ for degradation of exhaust gas in tunnels

https://doi.org/10.1515/gps-2021-0063
received May 19, 2021; accepted September 20, 2021

**Abstract:** To solve the environmental pollution caused by automobile exhaust in a tunnel, this study has developed a modified nano-$TiO_2$ based on $Fe^{3+}$ and $Ce^{3+}$. The modified nano-$TiO_2$ is prepared by the sol–gel method, and the modification adopts $Fe^{3+}$ single-doping, $Ce^{3+}$ sing-doping, and co-doping. The properties were also characterized by X-ray diffraction analysis, UV-vis diffuse reflectance analysis, fluorescence spectroscopy analysis, specific surface area analysis, and paramagnetic resonance popper analysis. The analyses showed that the doping of ions would change the energy band structure of nano-$TiO_2$ and produce crystal defects, thus improving the photocatalytic activity. Then, a self-fabricated exhaust gas degradation device was used to carry out the exhaust gas degradation experiments. The results showed that the modification improves the catalytic efficiency of nano-$TiO_2$, and $Fe^{3+}$, $Ce^{3+}$ co-doping > $Ce^{3+}$ single-doping > $Fe^{3+}$ single-doping > pure $TiO_2$. At the dosage of 0.5%, the maximum degradation efficiencies of NO and CO before compensation are 53.85% and 16.39%, respectively, and the maximum degradation rates are 1.04 and 0.93 $ppm \cdot min^{-1}$. After compensation, the maximum degradation efficiencies of NO and CO are 20.14% and 6.04%, respectively. The maximum degradation rate is 0.40 and 0.41 $ppm \cdot min^{-1}$, respectively.

**Keywords:** exhaust degradation, nano-$TiO_2$, metal ion modification, sol–gel method, degradation efficiency

## 1 Introduction

In 2017, the number of motor vehicles in China had reached 310 million, and the total emission of motor vehicle exhaust pollutants reached 43,597,000 tons. The substantial exhaust emissions will threaten human beings' living environment if not treated in time. The automobile exhaust mainly includes CO, HC, $NO_x$, $CO_2$, and CO and easily binds to hemoglobin which will cause human hypoxia. HC and $NO_x$ can form toxic fumes through the action of ultraviolet light, and can also cause discomforts, such as dizziness, chest tightness [1], and even cancer [2–4]. Nano-$TiO_2$ has the following advantages [5–7]: (i) low price, simple preparation equipment, and non-toxic; (ii) strong photocatalytic performance and strong redox ability; (iii) excellent chemical stability and corrosion resistance; (iv) suitable forbidden bandwidth (3.2 eV) and can effectively absorb ultraviolet light with wavelengths less than 387 nm in sunlight, etc. Therefore, compared with other catalysts, nano-$TiO_2$ has obvious advantages that make it the most widely used.

In 1972, Japanese scientists Fujishima and Honda [8] discovered that $TiO_2$ single-crystal electrodes could decompose water, which started the research on photocatalytic materials. In 1976, Frank [9,29] proposed that semiconductor materials could be used for photocatalytic degradation of organic pollutants, which opened the door to the application of photocatalytic materials. At the end of the 20th century, Japanese scholars [30] proposed the concept of the photocatalytic highway. They used various ways to improve the photocatalytic activity of nano-$TiO_2$, among which the main ones are surface noble metal deposition [31], surface photosensitization [32], composite semiconductors [33], ion doping, etc. [34]. Meng and Liu [35] sprayed a lipophilic permeate containing nano-$TiO_2$ into asphalt pavement. They have used scanning electron microscopy to observe the distribution of $TiO_2$ after

---

* **Corresponding author: Jianmin Wu,** Key Laboratory of Highway Engineering in Special Areas, Ministry of Education School of Highway, Chang'an University, Xian 710064, Shanxi, China, e-mail: wujm@chd.edu.cn
**Yin Luo:** Key Laboratory of Highway Engineering in Special Areas, Ministry of Education School of Highway, Chang'an University, Xian 710064, Shanxi, China, e-mail: 2019121136@chd.edu.cn
**Zhong Qin:** Key Laboratory of Highway Engineering in Special Areas, Ministry of Education School of Highway, Chang'an University, Xian 710064, Shanxi, China, e-mail: 2019121175@chd.edu.cn
**Hengcong Zhang:** Key Laboratory of Highway Engineering in Special Areas, Ministry of Education School of Highway, Chang'an University, Xian 710064, Shanxi, China, e-mail: 2019121171@chd.edu.cn

penetrating into the interior of the asphalt pavement voids. The effects of humidity, light intensity, and other factors on the photocatalytic efficiency of the eco-friendly asphalt pavement were investigated. The results showed that the catalytic efficiency first increased and then slightly decreased with the increase in air humidity, and the stronger the light and the shorter the wavelength, the higher the photocatalytic efficiency. Hassan et al. [36] studied the wear resistance of concrete pavements coated with $TiO_2$ photocatalysts and evaluated the effect of coated photocatalysts on the wear resistance of the concrete pavements by controlling the light intensity and air humidity to simulate different test environments. They have used scanning electron microscopy and energy electron spectroscopy to determine the concentration distribution of ions after $TiO_2$ coating, and high degradation efficiency of 26.9% was achieved for $NO_x$ removal at 5% of $TiO_2$ doping concentration. Vaiano et al. [37] used the sol–gel method to prepare N-doped nano-$TiO_2$ and loaded them onto glass microspheres to prepare coatings with photocatalytic functions. Larumbe et al. [38] used the sol–gel method to prepare N and Fe co-doped nano-$TiO_2$. They analyzed the effect of ion doping on the structure of nano-$TiO_2$, magnetic properties, and photocatalytic properties. Heather et al. [39] studied the degradation effect of concrete pavement coated with $TiO_2$ photocatalyst on $NO_x$. The results showed that the degradation effect was significant at an air relative humidity of 25%. Shang [10] used hot asphalt as a carrier to load photocatalytic materials so that they could adhere to the road surface or in the void, and achieve the purpose of decomposing $NO_x$ under the irradiation of visible light. Tan et al. [11] used doping to study the effect of exhaust gas degradation and investigated various road properties of doped asphalt mixes. The results showed that photocatalysts using doping hardly affect the multiple properties of asphalt mixes. Although nano-$TiO_2$ has many advantages as a photocatalyst, it has a wide energy bandgap. It can only use ultraviolet light in sunlight to trigger an electron leap. It does not absorb visible light, which accounts for 45% of sunlight [12,13], so the utilization of sunlight is extremely low.

In this study, for the poor ventilation conditions and low light intensity in the tunnel, a high-pressure sodium lamp with high penetrating power and high luminous efficiency is used as the light source, unlike the previous incandescent lamp. Based on the previous studies, $Fe^{3+}$ single doping, $Ce^{3+}$ single doping, and co-doping are used to modify the nano-$TiO_2$ to study the modification principle and effect of metal ions to achieve the adjustment of $TiO_2$ energy band structure, so that it can absorb and utilize visible light. X-ray diffraction (XRD) analysis shows that the doping of ions will reduce the size of nano-$TiO_2$. UV-Vis diffuse reflectance analysis shows that the doping of ions causes a significant redshift in the absorption band of nano-$TiO_2$. Fluorescence spectroscopy analysis shows that the doping of ions decreases the probability of electron-hole complexation. The specific surface area analysis shows that the doping of ions causes the pore size of nano-$TiO_2$ to become smaller and the surface area to increase. Paramagnetic resonance popper analysis shows that the doping of ions increases the number of electron-hole pairs and generates more reactive radicals. This experiment used AC-13 asphalt mixture rutting slabs to simulate tunnel pavement and then conducted tail gas degradation tests using a self-fabricated tail gas degradation device, which can simulate the tunnel environment to the maximum extent. The exhaust gas generation device is a standard exhaust gas tank, which can ensure the consistency of the initial concentration to the greatest extent, and compensate for the experimental error by using the blank group experiment. Finally, the best modifier and its optimal doping amount were determined to provide a method and basis for the subsequent photocatalyst modification research.

## 2 Materials and methods

### 2.1 Experimental reagents and experimental apparatus

The nano-$TiO_2$ and modified nano-$TiO_2$ were prepared by the sol–gel method [14–17,28]. The primary reagents were butyl titanate (analytical purity), anhydrous ethanol (superior purity), glacial acetic acid (analytical purity), deionized water (analytical purity), cerium chloride

**Table 1:** Experimental reagent and cost

| Experimental reagent | Butyl titanate/ 500 mL | Anhydrous ethanol/500 mL | Ice acetic acid/500 mL | Ferric chloride/500 g | Cerium chloride/25 g |
|---|---|---|---|---|---|
| Cost (yuan) | 33.00 | 28.00 | 33.00 | 37.24 | 37.00 |

(analytical purity), ferric chloride (analytical purity), etc. The central apparatus are constant temperature magnetic stirrer (HS-19), vacuum drying oven (DZF-6050), muffle furnace (SX2-2.5-10), etc. The costs of various reagents are shown in Table 1.

## 2.2 Experimental steps

The specific steps for the preparation of nano-$TiO_2$ and modified nano-$TiO_2$ by the sol–gel method are as follows:

1. 25 mL of anhydrous ethanol and 5 mL of glacial acetic acid was poured into a beaker at room temperature. Then, 17 mL of butyl titanate was slowly added with uniform stirring using a magnetic stirrer and stirred for 30 min to obtain a uniform and transparent light yellow solution A.
2. 20 mL of anhydrous ethanol, 5 mL of glacial acetic acid, and 10 mL of deionized water was thoroughly mixed at room temperature and a few drops of hydrochloric acid was added to control the pH of the solution between 2 and 3 to form solution B. Then, place it in a separatory funnel and set aside. Add 0.1%, 0.5%, and 1% of $Fe^{3+}$, $Ce^{3+}$ relative to the molar fraction of Ti atoms to make modified nano-$TiO_2$.
3. The solution B was slowly added (1–2 drops per second) to the solution A to obtain the sol under the action of a thermostatic magnetic stirrer at a controlled temperature of 30°C. Attention was paid so that the speed of the dropping was not be too fast to prevent the butyl titanate from hydrolyzing too fast, and the gel was obtained by aging for a while.
4. The gel was dried in a vacuum drying oven at 80°C for 24 h to get a dry gel.
5. The dry gel was crushed in a mortar and then placed in a muffle furnace and calcined at 500°C for 2 h to obtain nano-$TiO_2$. Nano-$TiO_2$ sols and nano-$TiO_2$ particles are shown in Figure 1.

The yield of nano-$TiO_2$ in the theoretical case is 4 g. The orthogonal experiments of nano-$TiO_2$ obtained under different conditions are given in Table 2.

The dissolution speed of butyl titanate is too fast and white flocculent is easily formed, while the dissolution speed is too slow and it is not easy to form a sol. Generally, the sol contains many tiny bubbles after it is made, and a series of chemical reactions will occur subsequently. Hence, it needs to be placed for a while to make the butyl titanate fully hydrolyzed. Calcination temperature and calcination time mainly affect the crystalline structure. When the temperature is 400°C, the crystalline form is mostly anatase phase, but the crystallization is not complete; when the temperature is 500°C, the crystalline form is completely anatase phase; when temperature increases, the material will be transformed from anatase phase to rutile phase, and the photocatalytic activity is reduced. With close to theoretical yield as the standard, the dissolution time of butyl titanate should be selected for 30 min, gel placed for 10 days, and calcination for 2 h at 500°C.

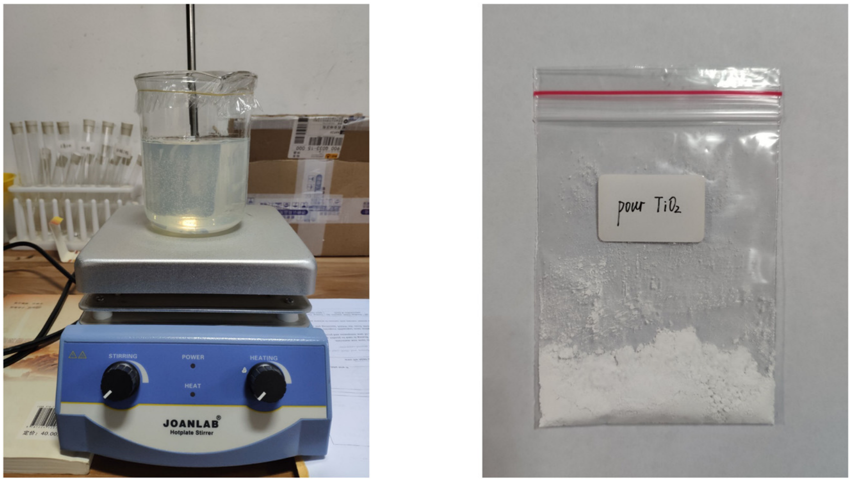

(a) (b)

**Figure 1:** (a) The sol of $TiO_2$ and (b) the particles of $TiO_2$.

**Table 2:** Orthogonal test table for preparation of $TiO_2$

| Serial number | Dissolution time of butyl titanate (min) | Gel placement time (days) | Calcination temperature (°C) | Calcination time (h) | Capacity (g) |
|---|---|---|---|---|---|
| 1 | 30 | 5 | 450 | 1 | 4.123 |
| 2 | 30 | 10 | 500 | 2 | 4.003 |
| 3 | 30 | 15 | 550 | 3 | 3.987 |
| 4 | 60 | 5 | 500 | 3 | 3.991 |
| 5 | 60 | 10 | 550 | 1 | 4.025 |
| 6 | 60 | 15 | 450 | 2 | 4.124 |
| 7 | 90 | 5 | 550 | 2 | 3.977 |
| 8 | 90 | 10 | 450 | 3 | 3.926 |
| 9 | 90 | 15 | 500 | 1 | 4.029 |

## 2.3 Photocatalytic principle

As a semiconductor material, the electronic energy level of nano-$TiO_2$ is discontinuous, in which there are empty energy level regions, so there are both full and empty bands. The bottom full band is called the valence band, the top empty band is called the conduction band, and the region from the top of the valence band to the bottom of the conduction band is called the forbidden band or bandgap. When the photoelectrons' energy is greater than or equal to the width of the forbidden band, the electrons in the valence band will be excited by light and jump to the conduction band, while the electrons in the valence band will generate holes due to the jump, forming electron-hole pairs. The electron-hole complex pair will be compounded under the action of an electric field and thus lose its activity. The electron-hole complex pair can react with $H_2O$ and $O_2$, which are on the surface of nano-$TiO_2$.

$$TiO_2 + h\gamma \rightarrow TiO_2 + h^+ + e^- \tag{1}$$

$$H_2O + h^+ \rightarrow {}^{\bullet}OH + H^+ \tag{2}$$

$$O_2 + e^- \rightarrow O_2^- \tag{3}$$

$$O_2 + H^+ \rightarrow HO_2 \tag{4}$$

$$2{}^{\bullet}HO_2 \rightarrow O_2^- + H_2O_2 \tag{5}$$

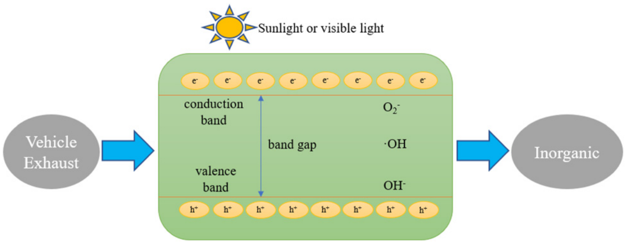

**Figure 2:** Schematic diagram of photocatalysis.

$$O_2^- + H_2O_2 \rightarrow {}^{\bullet}OH + OH^- \tag{6}$$

It can be seen from the above reactions that the electron-hole complex pair eventually generates superoxide ion radicals and hydroxyl radicals, which can oxidize CO and NO in the air into $CO_2$, various carbonates, nitrates, etc., due to the strongly oxidizing properties of these radicals, so as to achieve the purpose of degrading the car exhaust to cure the environment, and the specific catalytic principle is shown in Figure 2 [18].

## 2.4 Test systems

The P750 gas catalytic reaction device, which was developed by the Cusson Company in the United States, calculates the catalytic conversion efficiency by testing the change in the gas concentration (mainly refers to the harmful gas of automobile exhaust gas) flowing through the reactor. However, the equipment could not perform to its full efficiency when it is applied to test the catalytic decomposition performance of asphalt mixture on automobile exhaust gas, and the reason is that the equipment cannot provide the light conditions needed for the photocatalytic reaction [20]. The auto-exhaust reaction test equipment was developed independently by Tohoku Forestry University [21], which contains an automobile exhaust gas supply system, computer-aided test system, gas chamber, and other multi-functional components and structures, with a variety of sensors (such as oxygen sensor, carbon dioxide sensor, hydrocarbon sensor, carbon monoxide sensor, pressure box, temperature sensor, etc.). However, due to the instability of the sensor, the device has the disadvantages of unstable reading and short service life. In this study, the actual situation in the tunnel is combined with the disadvantages of poor lighting conditions and poor ventilation in the tunnel, so a closed

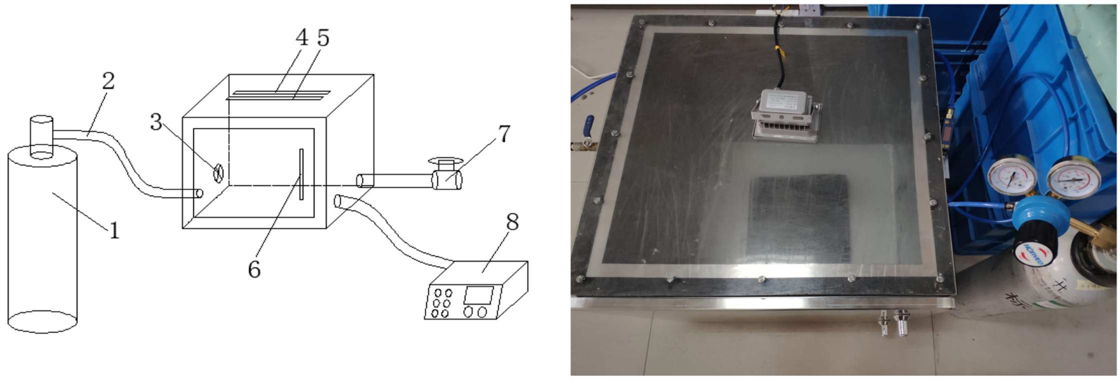

(a) (b)

**Figure 3:** (a) Degradation system design drawing and (b) exhaust gas degradation test system; (1) standard exhaust gas tank, (2) air inlet pipe, (3) small fan, (4) high pressure sodium lamp, (5) UV lamp, (6) sealed door, (7) exhaust gas cleaning device, and (8) exhaust gas analyzer.

chamber is used to simulate the tunnel, and the light is a high-pressure sodium lamp, which is commonly used in such low-light conditions in the tunnel due to its high luminous efficiency, low power consumption, long life, and high penetration [22]. The test device consists explicitly of three parts: a standard exhaust gas tank, a closed reaction chamber, and an exhaust gas analyzer, as shown in Figure 3.

## 2.5 Photocatalytic material specimen preparation

The coating type in this study uses a water coating solution. In the process of preparing the coating solution, it is easy to precipitate in the process of preparation as the specific gravity of nano-$TiO_2$ is 4.26, and nano-$TiO_2$ is easy to disperse unevenly in water and produce agglomeration. Therefore, during the preparation, a certain amount of dispersing stabilizer needs to be added, and the addition amount is 10–20% of the mass of nano-$TiO_2$. In the coating solution, water:nano-$TiO_2$:dispersion stabilizer = 1%:2%:0.4%. The specific laboratory preparation steps are as follows: (1) Weigh a certain amount of water, dispersant, and stabilizer. Add the dispersant and stabilizer to the aqueous solution, and shear at 500 rpm for 5 min with a high-speed shearer. (2) Add nano-$TiO_2$ to the above solution, and the water-based nano-$TiO_2$ coating solution can be produced by shearing at a high speed of 2,000 rpm for 30 min with a high-speed shearer [23,24].

In this study, relying on the actual needs of the project, the AC-13 asphalt mixture is used, fine aggregate is limestone, coarse aggregate is basalt, oil to stone ratio is 5.0%, 70# matrix asphalt is used, and the gradation design is as shown in Table 3.

The nano-$TiO_2$ coating solution and the specimens covered with photocatalytic materials are shown in Figure 4.

## 2.6 Evaluation indicators

Among the evaluation indices currently used to evaluate the performance of photocatalytic decomposition of vehicle exhaust, the cumulative decomposition rate (i.e., decomposition efficiency) is the most common evaluation index [25,26]. The cumulative decomposition rate is calculated in Eq. 7:

$$\eta = \frac{M_0 - M_1}{M_0} \times 100\% \tag{7}$$

**Table 3:** Gradation design

| Sieve hole (mm) | 16 | 13.2 | 9.5 | 4.75 | 2.36 | 1.18 | 0.6 | 0.3 | 0.15 | 0.075 |
|---|---|---|---|---|---|---|---|---|---|---|
| Target grading (%) | 100 | 96 | 77.5 | 49 | 32 | 21 | 15 | 10 | 7 | 5 |

(a) (b)

**Figure 4:** (a) The coating solution of nano-$TiO_2$ and (b) specimen covered with photocatalytic material.

where $\eta$ – cumulative decomposition rate, %; $M_0$ – initial concentration, ppm; and $M_1$ – final concentration, ppm.

The cumulative decomposition rate is one of the essential evaluation indicators for the reaction photocatalytic decomposition of automobile exhaust gas, as well as a quantitative indicator, but there are shortcomings that the indicator requires a fixed initial gas concentration of the test as well as a fixed closed reaction chamber.

In the process of photocatalytic degradation of automobile exhaust, the rate of gas concentration reduction is not always constant, which means that the gas concentration is not linearly related to time, so the decomposition rate is different at different periods. The average decomposition rate is an important index to react to different decomposition rates at different periods. The average decomposition rate is calculated in Eq. 8 [27]:

$$v = \frac{M_0 - M_1}{t} \tag{8}$$

where $v$ – average decomposition rate, ppm·min$^{-1}$; and $t$ – reaction time, min.

In this study, the average decomposition rate is differentiated based on the average decomposition rate, i.e., it is more time-sensitive. The concentration-time relationship graph is made with time as the horizontal coordinate and gas concentration as the vertical coordinate, which was then fitted by Origin to obtain the exhaust gas degradation curve, as shown in Figure 12. The slope of this curve indicates the decomposition rate.

# 3 Results and discussion

Nanomaterials are materials with at least one dimension in the nanoscale (1–100 nm) at the three-dimensional spatial scale, which is a typical mesoscopic system in the transition region at the junction of atomic clusters and macroscopic objects, neither microscopic nor macroscopic, with a series of specific physicochemical properties [19].

## 3.1 XRD

XRD uses the position and intensity of XRD diffraction angles to analyze the composition of minerals. It explores the phases of the substance based on the spacing of each crystal plane and the relative intensity of diffraction lines against PDF cards. By comparing the diffraction peaks of unknown substances with those of known substances, the various phases in the sample are derived. It can be

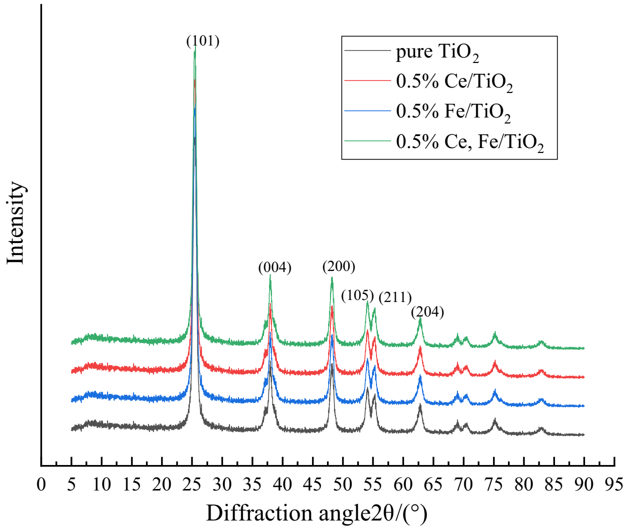

**Figure 5:** X-ray diffraction analysis.

derived from Figure 5 that the diffraction angles $2\theta = 25.3$, 37.9, 48.2, 54.1, 55.7, and 63.4, so the nano-$TiO_2$ is anatase crystalline type, and these diffraction peaks belong to (101), (004), (200), (105), (211), and (204), respectively. The determination of XRD crystal size is related to the peak width of the diffraction peak and the material grain size, which is calculated in Eq. 9:

$$D = \frac{K\lambda}{B\cos\theta} \tag{9}$$

where $D$ – grain size, nm; $K$ – Scherrer constant, generally taken as 0.89; $\lambda$ – wavelength of the rays, nm; $B$ – half-peak width of the diffraction peak, rad; and $\theta$ – Bragg diffraction angle, °.

This study used a DB-type X-ray diffractometer with the following technical parameters: Cu target K-α radiation ($\lambda$ = 1.5406 nm), operating voltage of 40 kV, operating current of 150 mA, scan range of 5–90°, and scan rate of $10°\cdot\text{min}^{-1}$. The calculation results of the relevant lattice parameters for different ion doping are displayed in Table 4.

As can be seen from Figure 5, the doping of $Fe^{3+}$ and $Ce^{3+}$ did not cause fundamental changes in the positions of the diffraction peaks of nano-$TiO_2$, which indicates that the modified nano-$TiO_2$ is still dominated by anatase. With the doping of ions, the diffraction peaks show specific regular changes. From Table 4, it can be concluded that the average grain size of $Ce^{3+}$, $Fe^{3+}$ co-doping is significantly smaller than that of pure $TiO_2$. The ionic radius of $Fe^{3+}$ is 0.064 nm and that of $Ti^{4+}$ is 0.068 nm, and the difference between the ionic radii is not large, indicating that part of $Fe^{3+}$ will replace $Ti^{4+}$ and exist in the crystal lattice during the doping modification process. The entry of $Fe^{3+}$ into the nano-$TiO_2$ lattice will destroy the periodicity of the crystal plasmon arrangement, thus inducing crystal distortion and inhibiting the growth of $TiO_2$ crystals. The ionic radius of $Ce^{3+}$ is 0.102 nm, which is much larger than that of $Ti^{4+}$, so the possibility of $Ce^{3+}$ entering the $TiO_2$ lattice to replace $Ti^{4+}$ is negligible, but it may exist at the $TiO_2$ grain boundary, i.e., the interface between two grains or microcrystals. On the one hand, it induces crystal distortion and form lattice defects. On the other hand, it will increase the diffusion energy barrier of atoms between grains and prevent direct contact between grains. Both of them will inhibit lattice growth, form lattice defects to trap photogenerated electrons, and reduce the probability of electron-hole complexation, thus improving photocatalytic activity.

**Table 4:** Calculation results of grain size of $TiO_2$ doped with different ions

| Parameters | Pure $TiO_2$ | 0.5% of $Fe/TiO_2$ | 0.5% of $Ce/TiO_2$ | 0.5% of Ce, $Fe/TiO_2$ |
|---|---|---|---|---|
| $D$ | 16.75 | 15.97 | 14.48 | 13.16 |
| $B$ | 0.4930 | 0.5056 | 0.5184 | 0.5213 |

## 3.2 UV-visible (UV-Vis) spectroscopy analysis

UV-Vis diffuse reflectance spectroscopy is the UV-Vis spectrum generated by using the degree of absorption of UV or visible light by the sample. This study used a UV 3600 Plus UV-Vis spectrophotometer with a scanning range of 200–900 nm.

The wavelengths of various kinds of light are composed of ultraviolet wavelength (below 400 nm), visible wavelength (400–760 nm), and infrared wavelength (above 760 nm). It can be seen from Figure 6 that the absorbance of nano-$TiO_2$ decreases with the increase in the wavelength of light, which decreases dramatically between the wavelengths of 350–450 nm. In this interval, the rate of decline first increases and then decreases, that is, there is an inflection point, making a tangent line at the point. The intersection of the tangent line and the horizontal coordinate can roughly represent the maximum value of the absorbance wavelength. The tangent line drawn for each spectrum in Figure 6 concludes that the doping of ions will increase the wavelength of $TiO_2$ response to visible light so that its absorption range is

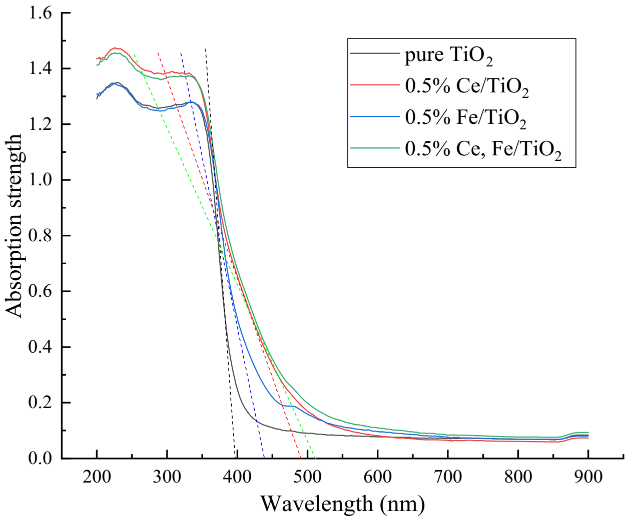

**Figure 6:** UV-Vis light diffuse reflection.

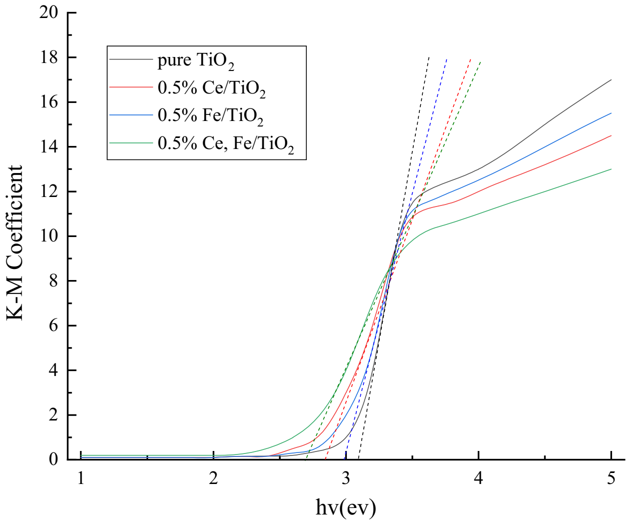

**Figure 7:** K–M conversion curve graph.

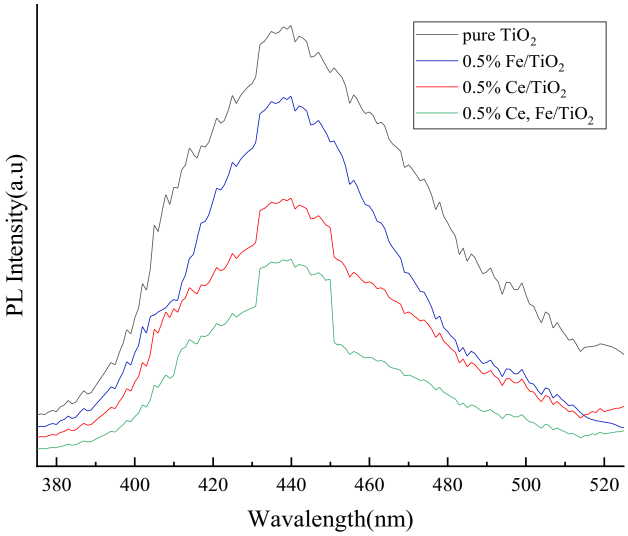

**Figure 8:** Fluorescence spectroscopy analysis.

expanded from ultraviolet light to visible light. The co-doping effect is better than $Ce^{3+}$ single doping and $Fe^{3+}$ single doping because the doping of ions inhibits the growth of $TiO_2$ nanocrystals and generates lattice defects, so that electron leap can occur even at low energy. The redshift of the sample's absorbed optical band is beneficial to excite the photocatalytic activity and form an electron-hole, thus improving the utilization of visible light.

To further investigate the effect of different ion doping on the forbidden bandwidth of nano-$TiO_2$, the optical band gap energy value of $TiO_2$ can be calculated after the Kubelka–Munk transformation of the UV-Vis diffuse absorption spectrum of $TiO_2$. The specific expression of the change is given by Eq. 10:

$$f(R_\infty) = \frac{(1 - R_\infty)^2}{2R_\infty} = \frac{k}{s} \tag{10}$$

where $R_\infty$ – reflectance; $s$ – scattering coefficient; and $k$ – molar absorption coefficient.

The relationship between the forbidden bandwidth of semiconductor materials and the wavelength of light absorption is given by Eq. 11:

$$E_g = \frac{1{,}024}{\lambda_g} \tag{11}$$

where $E_g$ – bandwidth and $\lambda_g$ – light absorption threshold.

After the K–M transformation of the UV-Vis diffuse reflectance absorption spectrum, the tangent line intersects with the horizontal axis and then the K–M transformation curve graph was obtained. It can be seen from Figure 7 that the absorption sidebands of the samples gradually move from the shortwave direction (390 nm) to the longwave direction (520 nm) with the doping of different ions, and the forbidden bandwidth decreases from 3.22 to 2.71 eV. This is related to the lattice distortion produced by $Fe^{3+}$ and $Ce^{3+}$, which causes defect traps on the $TiO_2$ surface and achieves the purpose of trapping photogenerated electron pairs. And according to the semiconductor energy band theory, the low-valent $Fe^{3+}$ replaces $Ti^{4+}$ in the lattice and forms a new d-energy band in the energy band gap of $TiO_2$. The d-energy band creates separated impurity energy levels in the forbidden band, leading to a decrease in the position of the bottom of the $TiO_2$ conduction band. The position of the $TiO_2$ conduction band bottom decreases so that the less energetic photons are excited to the impurity energy levels to trap electrons. This is consistent with the findings that ion doping can cause the UV-Vis absorption edge of $TiO_2$ to be redshifted.

## 3.3 PL analysis

Photoluminescence (PL) reflects the separation of electrons and holes. In general, the lower the intensity, the more efficient the separation of electrons and holes and the lower the probability of compounding. In this experiment, an FL4500 type fluorescence photometer was used for characterization and analysis. The PL spectra in the range of 375–525 nm were measured at an excitation wavelength of 365 nm, and as shown in Figure 8, the intensities of modified nano-$TiO_2$ were all lower than those of pure nano-$TiO_2$, indicating that the doping of modified ions induced crystal distortion and formed lattice defects, which produced traps for trapping photogenerated electrons and reduced the probability of electron-hole complexation. Among them, $Fe^{3+}$ and $Ce^{3+}$ co-doping has a lower electron-hole complex probability, indicating that the co-doping of two metal ions is more favorable to improve the catalytic efficiency of nano-$TiO_2$.

## 3.4 BET analysis

In chemical materials research, the biggest advantage of nanoscale photocatalytic materials over other macroscopic photocatalytic materials is that nanomaterials have a huge surface area and surface structure advantages. The specific surface area test referred to as the BET test method, has become the standard for qualitative analysis of adsorption properties of materials and microscopic particles in the field of materials research at home and abroad. Before the BET test analysis of composite nano photocatalytic materials, the sample needs to be subjected to nitrogen adsorption–desorption isothermal test and then the data are fitted and analyzed according to the BET formula, and the specific surface area and pore size of nano-$TiO_2$ and modified nano-$TiO_2$ are derived from the distribution data. As shown in Figure 9a, the modified nano-$TiO_2$ changed the linear type from type II to type IV compared with the pure $TiO_2$. It can be observed that the inflection point of modified nano-$TiO_2$ occurs between 0.55 and 0.75 relative pressure. After the inflection point, the rise rate decreases, and both show the absorption–desorption hysteresis phenomenon, indicating that the modified nano-$TiO_2$ belongs to the mesoporous material structure. This hysteresis phenomenon is caused by the presence of a large number of capillary pores on the surface, indicating that the doping of ions makes the catalyst surface more rough and porous with increased capillary structures. Figure 9b also reflects that the average pore size of modified nano-$TiO_2$ is smaller than that of pure $TiO_2$ and the specific surface area is larger than that of pure $TiO_2$, which further confirms the XRD analysis.

## 3.5 Electron spin resonance (ESR) analysis

In this thesis, ESR was used to monitor the formation of $^{\bullet}OH$. As shown in Figure 10, the area ratio of the four characteristic peaks was 1:2:2:1 under the high-pressure sodium lamp irradiation for 30 min, which belonged to the typical characteristic signal peaks of $^{\bullet}OH$, and all samples had obvious $^{\bullet}OH$ signal peaks. The ESR signals of modified nano-$TiO_2$ are stronger than those of pure $TiO_2$, which should be related to the number of separated electron-hole pairs. In general, more reactive radicals are beneficial to photocatalytic performance, which provides the possibility to subsequently enhance the tail gas degradation efficiency.

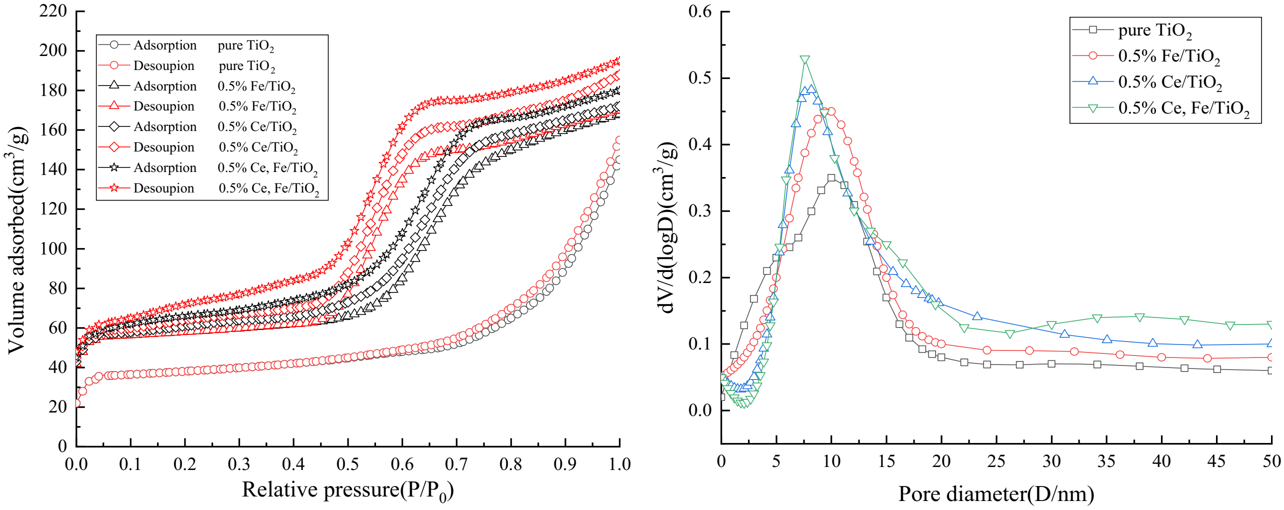

(a) (b)

**Figure 9:** (a) $N_2$ adsorption/desorption isotherms and (b) pore size distribution curves.

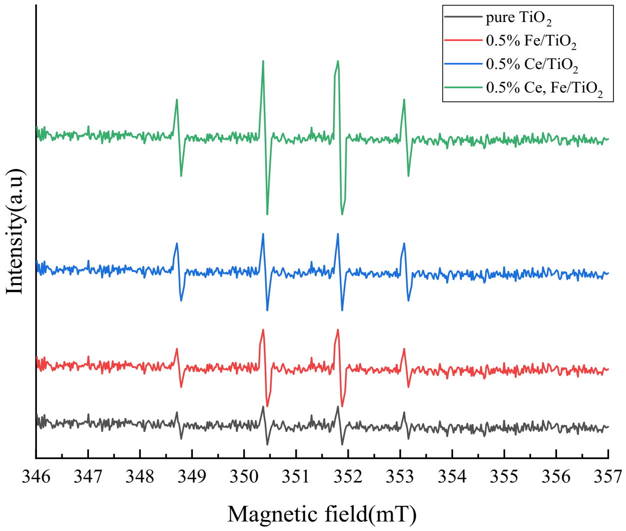

**Figure 10:** Results of electron spin resonance analysis.

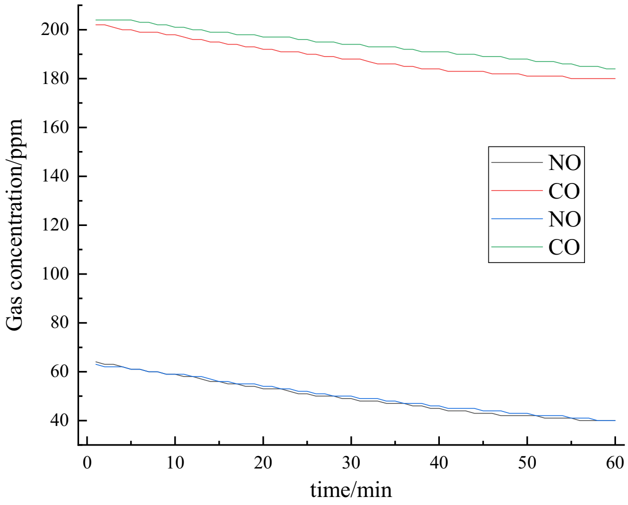

**Figure 11:** Graph of CO and NO concentration changes over time (blank test).

## 3.6 Exhaust degradation test

The source of exhaust gas for the test was a standard exhaust gas tank, and the composition ratio of the gas mixture was NO (40,560 ppm), CO (9.96%), $CO_2$ (5%), and $N_2$. The volume of the exhaust gas tank is 8 L, the length, width, and height of the sealed chamber are 60 cm, converted to a volume of 216 L. Using a microflow meter to control the volume of gas passing each time, the volume of gas mixture passed in the test is 0.5 L, and the initial gas concentration control range is shown in Table 5.

As can be seen from Table 5, the actual concentrations of CO and NO are less than the theoretical values, but the concentration of $CO_2$ is greater than the theoretical value. The reason for this is that in the process of the mixed gas entering the pipe, the connection between the pipes is not completely dense and part of the gas is left in the pipe, resulting in the actual concentration being less than the theoretical concentration. The increase in $CO_2$ concentration is due to the fact that the closed chamber is not a vacuum and contains air, which contains $CO_2$ in its composition, and when this content is greater than the loss value, it causes an increase in $CO_2$ content.

Before starting the test, the tightness of the reaction chamber should be checked to prevent large test errors. The airtightness was checked by not putting any specimen in the reaction chamber and then introducing 0.5 L of the gas mixture. The main objects of this test are CO and NO, and the concentration changes in CO and NO are tested within 60 min. To avoid the error brought by one group of tests, two groups of each test are done in this study, and the specific test results are shown in Figure 11.

As can be seen from Figure 11, the concentration of CO slightly decreases with the growth of time, while the concentration of NO significantly reduces with the growth of time. The reason is that part of NO has an oxidation reaction with $O_2$ in the air, so the concentration of CO slightly decreases and can be concluded that the airtightness of the confinement chamber is good and meets the requirements of the test.

After the airtightness check, debug and preheat the exhaust gas analyzer, then put the photocatalytic specimen into the sealed chamber, close the sealing door, start the exhaust gas analyzer, and open the pressure reducing valve of the exhaust gas tank after the analyzer indicates a stable number. The volume of the gas mixture

**Table 5:** Initial gas concentration control

| Gases (ppm) | CO | NO | $CO_2$ | Gases (ppm) | CO | NO | $CO_2$ |
|---|---|---|---|---|---|---|---|
| Theoretical concentration | 231.26 | 92.59 | 115.63 | Actual concentration | 202–212 | 62–72 | 214–229 |

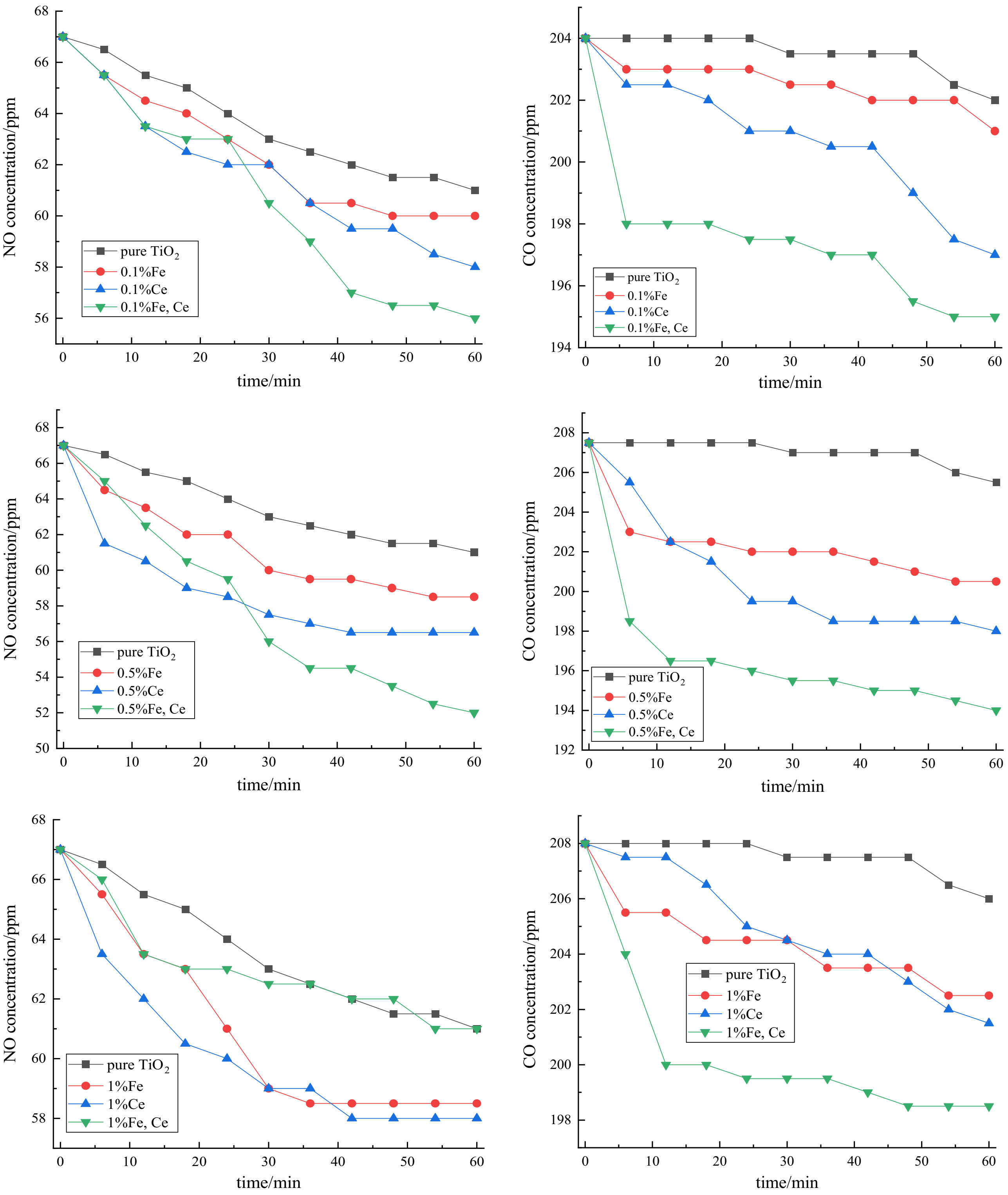

**Figure 12:** Graph of NO and CO concentration changes over time.

is controlled by the micro-flow meter, and the rate chosen by the micro-flow meter is 2 L·min$^{-1}$, i.e., the pressure reducing valve is closed after 15 s. Turn on the small fan and wait for 5 min to make the mixture evenly fill the sealed chamber, then turn on the high-pressure sodium lamp, set the parameters of the exhaust gas analyzer for a total duration of 60 min, because the exhaust gas analyzer is equipped with a data export function, the data export interval is set to 6 min per time. At the end of the test, turn off the fan, open the sealed door, and take out the test specimen after the exhaust gas is exhausted from the test system to prepare for the next test.

In the exhaust gas degradation test, the surface of the AC-13 asphalt mixture was pretreated first. Then, the prepared water-based nano-$TiO_2$ coating solution was sprayed onto the rutting plate at a dosage of 556 mL·m$^{-2}$, and it could be used in the exhaust gas degradation test after the water evaporated. A total of 20 groups were tested. The specific experimental data are shown in Table 6.

Because the airtightness of the closed chamber body is not completely sealed as well as the reason that NO will be naturally oxidized in the air, a blank test group is needed to make the correction comparison. The specific compensation method is: the initial concentration of the blank group is $C_0$, the concentration of the blank group is $C_1$, and the concentration of the test group is $C_2$, then the actual concentration of the test group after degradation is given by Eq. 12:

$$C = C_2 + C_0 - C_1 \tag{12}$$

After compensating the data of each group, the average value of two groups A and B was taken as the final test data, as shown in Figure 12.

It can be noted that the doping of ions will improve the degradation efficiency of the exhaust gas of nano-$TiO_2$ under high-pressure sodium lamp irradiation, and the degradation effect of co-doping is better than cerium ion single doping, better than iron ion single doping better than pure $TiO_2$, and the degradation efficiencies are shown in Tables 7 and 8.

The concentration curve of exhaust gas degradation was obtained by fitting with Origin software. The maximum value of the slope of the curve was found to represent the maximum value of the degradation rate of exhaust gas, and the categories from left to right in Table 8 were represented by $S_0$–$S_{10}$. The exhaust gas degradation rates of NO and CO are shown in Figure 13. The maximum values of the degradation rates of NO and CO were obtained as shown in Tables 9 and 10.

**Table 6:** Data of exhaust gas degradation test

| Grouping | | Group A | | | | | | Group B | | | | | |
|---|---|---|---|---|---|---|---|---|---|---|---|---|---|
| **Time** | **Min** | **0** | **12** | **24** | **36** | **48** | **60** | **0** | **12** | **24** | **36** | **48** | **60** |
| Blank test | NO | 63 | 58 | 51 | 47 | 42 | 40 | 64 | 58 | 52 | 47 | 43 | 40 |
| | CO | 202 | 198 | 193 | 188 | 185 | 182 | 203 | 198 | 194 | 189 | 185 | 182 |
| Pure $TiO_2$ | NO | 66 | 59 | 51 | 44 | 41 | 38 | 68 | 61 | 53 | 46 | 42 | 40 |
| | CO | 214 | 208 | 205 | 201 | 196 | 191 | 209 | 203 | 200 | 195 | 191 | 187 |
| 0.1% of Fe | NO | 67 | 59 | 51 | 44 | 39 | 36 | 64 | 56 | 48 | 41 | 36 | 34 |
| | CO | 195 | 189 | 183 | 180 | 177 | 173 | 205 | 199 | 192 | 189 | 186 | 183 |
| 0.5% of Fe | NO | 69 | 60 | 52 | 45 | 40 | 36 | 65 | 56 | 48 | 41 | 36 | 34 |
| | CO | 211 | 201 | 195 | 192 | 187 | 182 | 208 | 198 | 192 | 189 | 184 | 182 |
| 1% of Fe | NO | 67 | 58 | 50 | 44 | 39 | 36 | 69 | 60 | 50 | 42 | 37 | 36 |
| | CO | 209 | 201 | 195 | 192 | 187 | 182 | 207 | 199 | 194 | 191 | 185 | 182 |
| 0.1% of Ce | NO | 68 | 60 | 55 | 48 | 42 | 36 | 69 | 61 | 56 | 49 | 42 | 36 |
| | CO | 210 | 206 | 199 | 194 | 190 | 183 | 210 | 206 | 197 | 191 | 185 | 182 |
| 0.5% of Ce | NO | 65 | 54 | 47 | 41 | 36 | 32 | 68 | 55 | 45 | 39 | 34 | 33 |
| | CO | 207 | 198 | 190 | 185 | 182 | 178 | 208 | 198 | 191 | 184 | 180 | 177 |
| 1% of Ce | NO | 65 | 55 | 48 | 42 | 37 | 34 | 67 | 56 | 46 | 41 | 36 | 34 |
| | CO | 211 | 206 | 199 | 193 | 190 | 183 | 209 | 204 | 197 | 191 | 188 | 183 |
| 0.1% of Fe, Ce | NO | 69 | 60 | 55 | 48 | 39 | 35 | 69 | 60 | 51 | 41 | 36 | 34 |
| | CO | 204 | 191 | 187 | 183 | 178 | 175 | 204 | 190 | 185 | 183 | 178 | 174 |
| 0.5% of Fe, Ce | NO | 72 | 61 | 52 | 44 | 39 | 34 | 71 | 61 | 50 | 41 | 35 | 32 |
| | CO | 207 | 192 | 187 | 182 | 178 | 174 | 208 | 192 | 185 | 181 | 177 | 173 |
| 1% of Fe, Ce | NO | 62 | 53 | 46 | 41 | 36 | 32 | 61 | 52 | 45 | 40 | 35 | 32 |
| | CO | 210 | 197 | 192 | 188 | 182 | 179 | 209 | 197 | 192 | 186 | 183 | 180 |

**Table 7:** Exhaust gas degradation efficiency (NO)

| Degradation efficiency | Blank test | Pure $TiO_2$ | 0.1% of Fe | 0.5% of Fe | 1% of Fe | 0.1% of Ce | 0.5% of Ce | 1% of Ce | 0.1% of Fe, Ce | 0.5% of Fe, Ce | 1% of Fe, Ce |
|---|---|---|---|---|---|---|---|---|---|---|---|
| Before compensation | 37.01 | 41.79 | 46.57 | 47.76 | 47.06 | 47.45 | 51.13 | 48.49 | 50.00 | 53.85 | 47.97 |
| After compensation | — | 8.96 | 10.69 | 12.69 | 12.50 | 13.14 | 15.79 | 12.88 | 15.94 | 20.98 | 9.76 |

**Table 8:** Exhaust gas degradation efficiency (CO)

| Degradation efficiency | Blank test | Pure $TiO_2$ | 0.1% of Fe | 0.5% of Fe | 1% of Fe | 0.1% of Ce | 0.5% of Ce | 1% of Ce | 0.1% of Fe, Ce | 0.5% of Fe, Ce | 1% of Fe, Ce |
|---|---|---|---|---|---|---|---|---|---|---|---|
| Before compensation | 10.12 | 10.64 | 11.00 | 13.13 | 12.50 | 13.10 | 14.46 | 12.86 | 14.46 | 16.39 | 14.32 |
| After compensation | — | 0.95 | 1.50 | 3.34 | 2.64 | 3.33 | 4.58 | 3.10 | 4.41 | 6.51 | 4.53 |

**Table 9:** Exhaust gas degradation rate (NO)

| Degradation rate | Blank test | Pure $TiO_2$ | 0.1% of Fe | 0.5% of Fe | 1% of Fe | 0.1% of Ce | 0.5% of Ce | 1% of Ce | 0.1% of Fe, Ce | 0.5% of Fe, Ce | 1% of Fe, Ce |
|---|---|---|---|---|---|---|---|---|---|---|---|
| Before compensation | 0.58 | 0.79 | 0.80 | 0.85 | 0.94 | 0.57 | 0.98 | 0.95 | 0.84 | 1.04 | 0.75 |
| After compensation | — | 0.20 | 0.21 | 0.25 | 0.25 | 0.27 | 0.25 | 0.25 | 0.28 | 0.40 | 0.14 |

**Table 10:** Exhaust gas degradation rate (CO)

| Degradation rate | Blank test | Pure $TiO_2$ | 0.1% of Fe | 0.5% of Fe | 1% of Fe | 0.1% of Ce | 0.5% of Ce | 1% of Ce | 0.1% of Fe, Ce | 0.5% of Fe, Ce | 1% of Fe, Ce |
|---|---|---|---|---|---|---|---|---|---|---|---|
| Before compensation | 0.46 | 0.36 | 0.53 | 0.69 | 0.57 | 0.52 | 0.85 | 0.57 | 0.75 | 0.93 | 0.83 |
| After compensation | — | 0.12 | 0.05 | 0.19 | 0.12 | 0.23 | 0.36 | 0.11 | 0.29 | 0.41 | 0.34 |

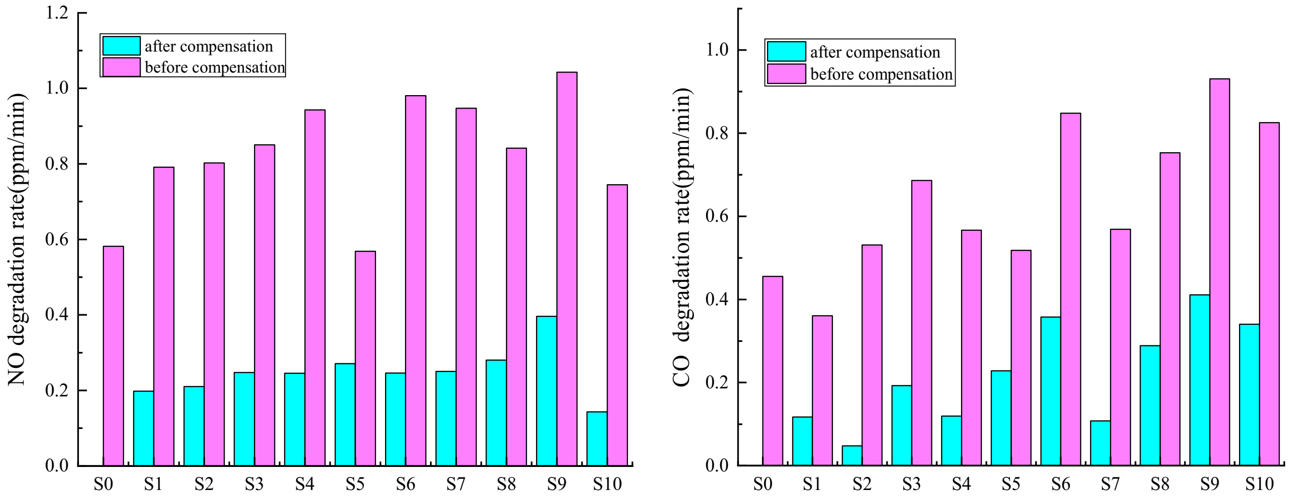

**Figure 13:** Exhaust gas degradation rate of NO and CO.

It can be noted from exhaust gas degradation test that the degradation effect of $Ce^{3+}$, $Fe^{3+}$ co-doping is better than $Ce^{3+}$ single doping, $Fe^{3+}$ single doping and pure $TiO_2$, where the maximum degradation efficiency and maximum degradation rate are $Ce^{3+}$, $Fe^{3+}$ co-doping, and the doping amount is 0.5%. This is because in the process of doping, $Fe^{3+}$ with a small ion radius replaces part of $Ti^{4+}$ and thus changes the crystal structure, while $Ce^{3+}$ with a large ion radius exists at the grain boundary position and increases the diffusion energy barrier between the grains, both of which can induce lattice distortion, form lattice defects, reduce the probability of electron-hole complexation, improve photocatalytic activity, and thus improve the exhaust gas degradation efficiency. But too much ion doping will cause the remaining ions to accumulate on the particle surface of the catalyst, resulting in a reduced contact area between nano-$TiO_2$ and visible light, thus decreasing the catalytic activity.

## 4 Conclusion

In conclusion, the efficiency of exhaust gas degradation efficiency of nano-$TiO_2$ with different ion doping for use in tunnels is investigated. The two ions differ in the principle of increasing photocatalytic activity: $Fe^{3+}$ is in the form of substituted $Ti^{4+}$, while $Ce^{3+}$ is present at the grain boundary sites, increasing the diffusion energy barrier. The doping of different ions will improve the degradation efficiency of nano-$TiO_2$ exhaust gas under a high-pressure sodium lamp, and the degradation efficiency is: $Fe^{3+}$, $Ce^{3+}$ co-doping > $Ce^{3+}$ single doping > $Fe^{3+}$ single doping > pure $TiO_2$. The maximum degradation efficiency and maximum degradation rate were of $Fe^{3+}$, $Ce^{3+}$ co-doped, and the doping amount was 0.5%. The maximum degradation efficiencies of NO and CO before compensation were 53.85% and 16.39%, respectively, and the maximum degradation rates were 1.04 and 0.93 $ppm \cdot min^{-1}$. The maximum degradation efficiencies of NO and CO after compensation were 20.14% and 6.04%, with top degradation rates of 0.40 and 0.41 $ppm \cdot min^{-1}$.

The use of the in-tunnel exhaust gas degradation materials prepared in this study for practical engineering purposes requires further research. In this study, an aqueous solution coating is used, and further research is needed on how to make a highly durable and waterproof coating subsequently. The optimal amount of co-doping is 0.5%, and the molar fraction ratio of 1:1 is used for co-doping. The specific molar fraction ratio of the two to achieve the best photocatalytic performance of $TiO_2$ nanomaterials remains to be investigated.

**Acknowledgements:** We thank Mr Jianmin Wu from Chang'an University for his suggestions on this article. We thank all the participants in this study.

**Funding information:** Science and Technology Project of Guangxi Zhuang Autonomous Region Transportation Department.

**Author contributions:** Yin Luo: writing – original draft and experiment; Jianmin Wu: writing – review and editing; Hengcong Zhang: experiment; Zhong Qin: experiment.

**Conflict of interest:** Authors state no conflict of interest.

**Data availability statement:** All data generated or analyzed during this study are also available from the corresponding author on reasonable request.

## References

[1] Barolo G, Livraghi S, Chiesa M, Paganini MC, Giamello E. Mechanism of the photoactivity under visible light of N-doped titanium dioxide. Charge carriers migration in irradiated N-$TiO_2$ investigated by electron paramagnetic resonance. J Phys Chem C. 2012;116(39):20887–994. doi: 10.1021/jp306123d.

[2] Burkardt A, Weisweiler W, Tillaart J, Schfer-Sindlinger A, Lox ES. Influence of the $V_2O_5$ loading on the structure and activity of $V_2O_5/TiO_2$ SCR catalysts for vehicle application. Top Catal. 2001;16–17(1):369–75. doi: 10.1023/A:1016673418398.

[3] Zhu J, Birgisson B, Kringos N. Polymer modification of bitumen: advances and challenges. Eur Polym J. 2014;54(1):18–38. doi: 10.1016/j.eurpolymj.2014.02.005.

[4] Yin S, Ihara K, Aita Y, Komatsu M, Sato T. Visible-light induced photocatalytic activity of $TiO_2$xAy (A = N, S) prepared by precipitation route. J Photoch Photobio A. 2006;179(1):105–14. doi: 10.1016/j.jphotochem.2005.08.001.

[5] Schmitt M, Dylla H, Hassan MM, Mohammad LN, Rupnow T, Wright E. Impact of mixed nitrogen dioxide ($NO_2$) and nitrogen oxide (NO) gases on titanium dioxide photodegradation of $NO_x$. Transportation and Development Institute Congress 2011: Integrated Transportation and Development for a Better Tomorrow; 2011. p. 731–40.

[6] Nan Z, Ye M, Wen X, Lin C. Rutile $TiO_2$ nanosheet arrays planted on magnetron sputtered Ti metal layers for efficient Perovskite solar cells. J Electrochem. 2017;23(2):226–37.

[7] Rettie A, Klavetter KC, Lin JF, Dolocan A, Mullins CB. Improved visible light harvesting of $WO_3$ by incorporation of sulfur or iodine: a tale of two impurities. Chem Mater. 2014;26(4):1670–7. doi: 10.1021/cm403969r.

[8] Fujishima A, Honda K. Photolysis-decomposition of water at the surface of an irradiated semiconductor. Nature. 1972;238(5385):37–8. doi: 10.1038/238037a0.

[9] Frank LA, Ackerson KL, Lepping R. On hot tenuous plasmas, fireballs, and boundary layers in the earth, s magnetotail. J Geophys Res. 1976;81(34):5859–81. doi: 10.1029/JA083iA07p03358.

[10] Shang PD. Application of asphalt concrete pavement that can degrade automobile exhaust in tunnels. Highway. 2014;59(3):189–92. doi: CNKI:SUN:GLGL.0.2014-03-044.

[11] Tan YQ, Li LK, Wei P, Sun Z. Application performance evaluation of biodegradable automobile exhaust materials in asphalt pavement. China J Highw Transp. 2010;23(6):21–7. doi: CNKI:SUN:ZGGL.0.2010-06-005.

[12] Wang H, Xu Q, Zheng X, Han W, Zheng J, Jiang B, et al. Synthesis mechanism, enhanced visible-light-photocatalytic properties, and photogenerated hydroxyl radicals of PS@CdS core–shell nanohybrids. J Nanopart Res. 2014;16(12):1–15. doi: 10.1007/s11051-014-2794-3.

[13] Choi W, Termin A, Hoffmann MR. The role of metal ion Dopants in quantum-sized $TiO_2$: correlation between photoreactivity and charge carrier recombination dynamics. J Phys Chem-US. 1994;98(51):13669–79. doi: 10.1021/j100102a038.

[14] Hamad D, Dhib R, Mehrvar M. Photochemical degradation of aqueous polyvinyl alcohol in a continuous UV/$H_2O_2$ process: experimental and statistical analysis. J Polym Env. 2016;24(1):72–83. doi: 10.1007/s10924-016-0750-2.

[15] Kanan S, Moyet MA, Arthur RB, Patterson HH. Recent advances on $TiO_2$-based photocatalysts toward the degradation of pesticides and major organic pollutants from water bodies. Catal Rev. 2019;62(3):1–65. doi: 10.1080/01614940.2019.1613323.

[16] Byrne C, Moran L, Hermosilla D, Merayo N, Ángeles B, Stephen R, et al. Effect of Cu doping on the anatase-to-rutile phase transition in $TiO_2$ photocatalysts: theory and experiments. Appl Catal B-Environ. 2019;246(6):266–76. doi: 10.1016/j.apcatb.2019.01.058.

[17] Adhikari SP, Awasthi GP, Kim HJ, Park CH, Kim CS. Electrospinning directly synthesized porous $TiO_2$ nanofibers modified by graphitic carbon nitride sheets for enhanced photocatalytic degradation activity under solar light irradiation. Langmuir Acs J Surf Colloids. 2016;32(24):6163–75. doi: 10.1021/acs.langmuir.6b01085.

[18] Chao W, Ao Y, Wang P, Hou J, Qian J, Zhang S. Preparation, characterization, photocatalytic properties of titania hollow sphere doped with cerium. J Hazard Mater. 2010;178(1–3):517–21. doi: 10.1016/j.jhazmat.2010.01.111.

[19] Asadi S, Hassan M, Nadiri A, Dylla H. Artificial intelligence modeling to evaluate field performance of photocatalytic asphalt pavement for ambient air purification. Env sci Pollut Res Int. 2014;21(14):8847–57. doi: 10.1007/s11356-014-2821-z.

[20] Osborn D, Hassan M, Asadi S, White JR. Durability quantification of $TiO_2$ surface coating on concrete and asphalt pavements. J Mater Civ Eng. 2014;26(2):331–7. doi: 10.1061/(ASCE)MT.1943-5533.0000816.

[21] Han XC, Du XJ, Li HG. Design of test system for automobile exhaust degradation material test chamber. Forestry Machinery Woodworking Equip. 2005;7:24–6. doi: 10.3969/j.issn.2095-2953.2005.07.009.

[22] Zhang JP. Comparison and selection of high-pressure sodium lamps and LED lamps in urban road lighting. Electr Technol Intell Build. 2019;13(4):25–6. doi: CNKI:SUN:ZNDQ.0.2019-04-007.

[23] Ruzi P. Environmental-friendly pavement technology for exhaust gas absorption in tunnels. China Highw. 2018;4:105–7. doi: CNKI:SUN:GLZG.0.2018-04-058.

[24] Xu YH, Gu GB, Chen XQ, Li XJ. Preparation, characterization and photocatalytic activity of composite nano-$Fe_2O_3/TiO_2$. J South China Univ Technol (Nat Sci.). 2001;11:76–80. doi: 10.3321/j.issn:1000-565X.2001.11.018.

[25] Wang ZL, Li M, Liu TX, Chang JZ, Shi HZ, Zhang ZJ, et al. Study on the photosensitization and sterilization activity of $TiO_2$ film. J Shaanxi Norm Univ (Nat Sci Ed). 2002;3:87–9. doi: 10.3321/j.issn:1672-4291.2002.03.019.

[26] Wang CY, Liu CY, Shen T. Surface modification of semiconductor photocatalysts. Chem J Chin Universities (Nat Sci Ed). 1998;19(12):2013–9. doi: CNKI:SUN:GDXH.0.1998-12-030.

[27] Gandhe AR, Fernandes JB. A simple method to synthesize N-doped rutile titania with enhanced photocatalytic activity in

sunlight. J Solid State Chem. 2005;178(9):2953–7. doi: 10.1016/j.jssc.2005.06.034.

[28] Katsumata H, Higashi F, Kobayashi Y, Tateishi I, Kaneco S. Dual-defect-modified graphitic carbon nitride with boosted photocatalytic activity under visible light. Sci Rep-UK. 2019;9(1):1–10. doi: 10.1038/s41598-019-49949-6.

[29] Durán-Álvarez JC, Santiago AL, Ramírez-Ortega D, Acevedo-Peña P, Castillón F, Ramírez-Zamora RM, et al. Surface modification of B–$TiO_2$ by deposition of Au nanoparticles to increase its photocatalytic activity under simulated sunlight irradiation. J Sol–Gel Sci Techn. 2018;88:474–87. doi: 10.1007/s10971-018-4815-7.

[30] Zhang KX. Current status and prospects of application of titanium dioxide photocatalyst technology in Japan. Tokyo: Xinhua News Agency; 1999.

[31] Gelover S, Mondragón P, Jiménez A. Titanium dioxide sol–gel deposited over glass and its application as a photocatalyst for water decontamination. J Photoch Photobio A. 2004;165(1–3):241–6. doi: 10.1016/j.jphotochem.2004.03.023.

[32] Hao LY, Mao LQ, Zhang SL, Dang HX, Li QL. Study on surface state and photocatalytic property of the compound semiconductor CdS/$TiO_2$. J Henan Univ (Nat Sci). 2004;34(2):28–32. doi: 10.1016/j.jco. 2003.08.015.

[33] Vinodgopal K, Kamat PV. Enhanced rates of photocatalytic degradation of an Azo dye using $SnO_2$/$TiO_2$ coupled semiconductor thin films. Env Sci Technol. 1995;29(3):841. doi: 10.1021/es00003a037.

[34] Vaiano V, Sacco O, Sannino D, Ciambelli P. Photocatalytic removal of spiramycin from wastewater under visible light with N-doped $TiO_2$, photocatalysts. Chem Eng J. 2015;261:3–8. doi: 10.1016/j.cej.2014.02.071.

[35] Meng C, Liu Y. $NO_x$ removal from vehicle emissions by functionality surface of asphalt road. J Hazard Mater. 2010;3(174):375–9. doi: 10.1016/j.jhazmat.2009.09.062.

[36] Hassan MM, Dylla H, Mohammad LN, Rupnow T. Evaluation of the durability of titanium dioxide photocatalyst coating for concrete pavement. Constr Build Mater. 2010;8(24):1456–61. doi: 10.1016/j.conbuildmat.2010.01.009.

[37] Vaiano V, Sacco O, Sannino D, Ciambelli P. Nanostructured N-doped $TiO_2$, coated on glass spheres for the photocatalytic removal of organic dyes under UV or visible light irradiation. Appl Catal B-Environ. 2015;171:153–61. doi: 10.1016/j.apcatb.2015.01.039.

[38] Larumbe S, Monge M, Gómez-Polo C. Comparative study of (N, Fe) doped $TiO_2$, photocatalysts. Appl Surf Sci. 2015;327:490–7. doi: 10.1016/j.apsusc.2014.11.137.

[39] Heather D, Marwa MH, Marion S, Tyson R, Louay NM. J Mater Civ Eng. 2011;23(7):1087–93. doi: 10.1061/(ASCE)MT.1943-5533.0000248.